Incompressible spatially-developing free-shear flows

By J. C. Buell

1. Introduction

The understanding of the role of large-scale structures and the process of mixing in free shear layers has advanced rapidly since the ground-breaking work of Brown & Roshko (1974). Until recently, most of the advances came from experimental projects such as those of Konrad (1976), Bernal (1981), and Mungal & Dimotakis (1984) in gaseous layers, and Koochesfahani & Dimotakis (1986) and Lasheras *et al.* (1986) in liquid layers. For a review, the reader is referred to the article by Ho & Huerre (1984). From the visualizations given in these papers one can see the spanwise rollers, their pairings, and the geometry of the streamwise vortices (called "ribs" here). As valuable as these experiments are for investigating certain aspects of mixing layers, it is very difficult to obtain quantitative information from them about the dynamics of three-dimensional (3-D) vortical structures. Numerical simulations, on the other hand, are ideal for obtaining detailed information under well-controlled conditions. Of course, there are disadvantages, usually related to limits on the Reynolds number or on the size of the domain. Several researchers (*e.g.*, Comte *et al.* 1987, Davis & Moore 1985, and Lowery 1986) have recently simulated spatially-developing mixing layers with the goal of extracting more information than is possible in experiments. These efforts were successful to some degree, but they all suffered from either too much diffusion (either physical or numerical) or lack of resolution.

The first goal of this research is to understand the dynamics of three-dimensional vortical structures, especially the interaction of the ribs and 2-D rollers. Because of vortex stretching effects, this requires accurate and well-resolved simulations. Another goal is to distinguish temporally- and spatially-growing shear layers in terms of the dynamics and observed vortical structures. This is important since the former is much easier to compute, but the error incurred in using temporal results for certain applications is unknown. The third goal is to investigate the effects of asymmetry on passive scalar mixing and fast-chemistry product formation. In this report, a brief summary of a new numerical method is presented, followed by results for mixing layer and wake flows.

2. Numerical method

In this section we briefly describe a new algorithm for approximately solving incompressible spatially-developing free-shear problems on a domain that is infinite in the vertical (y) direction and finite in the streamwise (x) and spanwise (z)

directions. The numerical method is analyzed in more detail elsewhere (Buell 1989).

The total velocity field $\mathbf{U} = (U, V, W)$ is decomposed using

$$\begin{aligned} U(x,y,z,t) &= U_0(y) + x\,U_e(y) + u(x,y,z,t), \\ V(x,y,z,t) &= V_e(y) + v(x,y,z,t), \\ W(x,y,z,t) &= w(x,y,z,t), \end{aligned}$$

so that all components of the perturbation variable $\mathbf{u}$ satisfy homogeneous boundary conditions at infinity. Here, V_e is some smooth function that tends to the entrainment values at $\pm\infty$ but is otherwise arbitrary, $U_e = -\partial V_e/\partial y$, and $U_0(y)$ is the mean velocity profile at the inflow (*e.g.*, a tanh profile for mixing layers, Gaussian for wakes). The Navier-Stokes equations are cast in fourth-order form by operating on the momentum equations with $\nabla\times$ and $\nabla\times\nabla\times$, and taking the streamwise components of both. The pressure is thus eliminated and dynamical equations for the perturbation streamwise velocity and vorticity result:

$$\frac{\partial}{\partial t}\nabla^2 u = \nabla_\perp^2 H_1 - \frac{\partial^2}{\partial x \partial y} H_2 - \frac{\partial^2}{\partial x \partial z} H_3 + \frac{1}{Re}\nabla^4 U, \tag{1}$$

$$\frac{\partial}{\partial t}\omega_1 = \frac{\partial}{\partial y} H_3 - \frac{\partial}{\partial z} H_2 + \frac{1}{Re}\nabla^2 \omega_1, \tag{2}$$

where $\mathbf{H} = \mathbf{U} \times \boldsymbol{\omega}$ and the "perpendicular" Laplacian is $\nabla_\perp^2 = \partial^2/\partial y^2 + \partial^2/\partial z^2$. For mixing layers, lengths have been scaled with the inflow vorticity thickness δ_ω (the half-width for wakes) and velocities with the freestream velocity difference $U_1 - U_2$ (freestream velocity for wakes). The Reynolds number based on these scales is thus $(U_1 - U_2)\delta_\omega/\nu$. The other two nondimensional parameters of the problem are the velocity ratio $r = U_2/U_1$ (velocity deficit for wakes) and the Schmidt number $Sc = \nu/D$ where D is the diffusion coefficient of the passive scalar.

After (1) and (2) are advanced in time, the vertical and spanwise velocities v and w are recovered directly from the continuity equation and the definition of ω_1. There are two main advantages in casting the governing equations in this form. First, only two dynamical equations need to be advanced in time instead of three. Second, unlike primitive variable methods, we may allow a difference to exist (consistent with the overall accuracy of the method) between the numerical divergence of the gradient and the Laplacian operator in the Poisson equation (1). This is because we invert the continuity equation directly instead of relying on the gradient of the pressure to ensure exact conservation of mass. The second point is very important since it introduces great flexibility in the choice of numerical approximations to various operators.

Equations (1) and (2) are advanced in time explicitly using a compact third-order Runge-Kutta scheme (Wray 1988). Since the Laplacian is contained in the

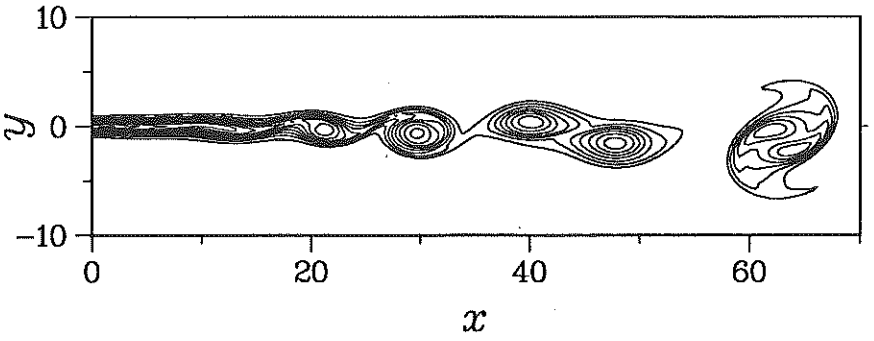

FIGURE 1. Contours of $-\omega_3$ for a 2-D mixing layer, $Re = 200$, $r = 0.2$. Contour interval is 0.1.

time-derivative term, a Poisson equation must be solved during each substep. The dependent variables are expanded in cosine (u, w) or sine (v, ω_1) series in a mapped vertical coordinate ζ (where $y = -\beta\cot(\pi\zeta)$ maps $[-\infty, \infty]$ to $[0, 1]$), and periodic Fourier series in z. The first x-derivatives in the continuity equation and in the advection terms are approximated with modified Padé finite differencing (Lele 1989). The particular approximation used here yields sixth-order accuracy for the low to moderate wavenumber components of the solution, and significantly lower dispersion errors for high wavenumbers. The second x-derivative is approximated also with a new Padé formula due to Lele (1989).

Dirichlet boundary conditions are specified for $\mathbf{u} = (u, v, w)$ at the inflow. Typically, 2-D Rayleigh equation eigenfunction profiles for a frequency near the most unstable one are used for u and v, and 3-D steady profiles for v and w are added to produce streamwise vortices. At the exit, each velocity component is required to satisfy a "convective" outflow boundary condition of the form $\partial\psi/\partial t = -c\,\partial\psi/\partial x$, where c is the nominal speed of the large structures. At infinity, $\mathbf{u} = 0$. For the mixing layer simulations, we used $V_e(y = -\infty) = .004$ and $V_e(y = \infty) = -.01$. These values were chosen to minimize the streamwise pressure gradient outside of the shear layer (this is analogous to experiments where the walls of the wind tunnel are adjusted inward).

3. Mixing layers

3.1. Dynamics of vortical structures

Our base-line case is a two-dimensional flow at $Re = 200$ and $r = 0.2$. This simulation was performed on a 192×128 mesh (grid points in x, modes in y, respectively) with 144 collocation points in y for partial dealiasing. The domain length in the streamwise direction is 70, and the vertical mapping parameter is $\beta = 8$. The layer was forced at a fundamental frequency of 0.5, although the most amplified frequency at the inflow is 0.65. This was done to compensate for the viscous thickening of the layer a short distance downstream.

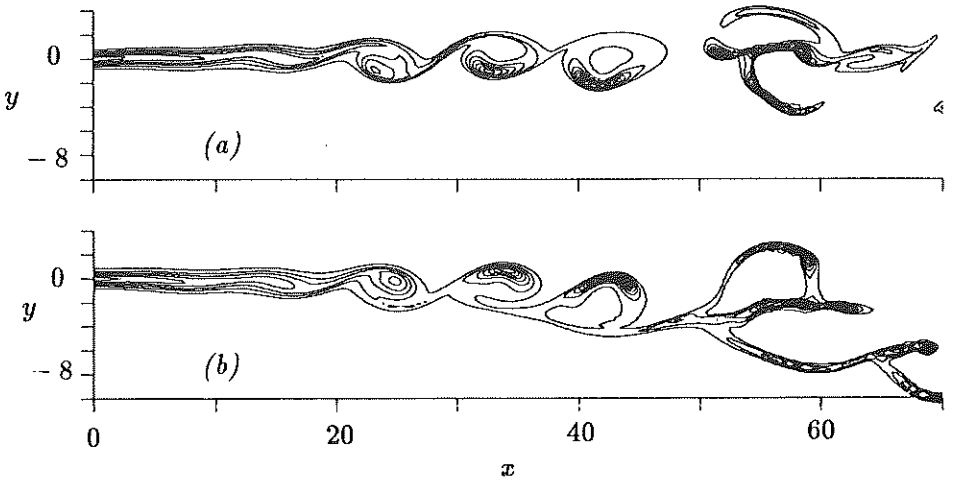

FIGURE 2. Contours of $-\omega_3$ for a 3-D mixing layer, $Re = 200$, $r = 0.2$. *(a)* $z = 0$, *(b)* $z = 2.75$. Contour interval is 0.15.

Shown in Fig. 1 are contours of vorticity (ω_3) where the fundamental was forced at an amplitude of 0.01 and the subharmonic at 0.005. The former leads to rollup and the latter to pairing of the vortices. The resulting flowfield is periodic in time with a weak nonperiodic component due to the feedback from the outflow boundary condition (Buell & Huerre 1988). The organized nature of the inflow forcing creates a "stairstep" growth of the layer downstream, where we find a high growth rate during the rollup and pairing, and small or nonexistent growth in the saturated region between.

To examine the effects of three-dimensionality, a pair of counter-rotating streamwise vortices are added at the inflow with maximum vorticity set to 5% of the maximum slope of $U_0(y)$. Between each vortex and its neighbor to either side is a symmetry plane where $\omega_1 = 0$. The Reynolds number and velocity ratio is the same as before. We set the spanwise wavelength to 5.5, or 58% of the streamwise wavelength of the rollers. This is consistent with both experiment (Huang & Ho 1989) and theory (Pierrehumbert & Widnall 1982). Due to the larger gradients that arise in the 3-D case, a finer grid was used, $256\times144\times24$ with a $y\times z$ collocation grid of 192×32 to reduce aliasing errors.

Shown in Fig. 2 are contours of spanwise vorticity (ω_3) in the two x-y symmetry planes. These plots show the initial laminar layer, development of 2-D rollers, and 3-D cup-like structures. The amplitude of the vorticity in the "cups" reaches about twice that of the maximum vorticity in the inflow profile U_0.

A 3-D visualization of the streamwise vortices (called "ribs") is shown in Fig. 3. Shown also are opposite-signed streamwise vortices inside the rollers. Note that the first pair of ribs is almost straight and nearly parallel, but the second pair is distorted and not parallel. The latter pair is very similar to the structures observed by Lasheras *et al.* (1986) in their low Reynolds number experiments in

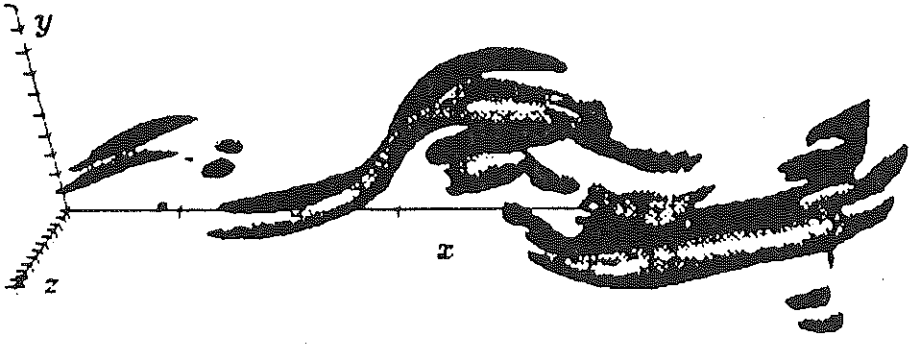

FIGURE 3. Perspective view of ω_1, contour levels ± 0.6.

water. This distortion is apparently due to self-induction effects between the ribs and the opposite-signed streamwise-vorticity structures inside the downstream roller. The ribs are intensified by the 2-D strain field of the main rollers, but this mechanism cannot increase the circulation around a rib. However, since the radius of the ribs remains about constant (or grows), the circulation increases significantly. The mechanism for this is the "conversion" of ω_3 into ω_1 by one of the "vortex stretching" terms in (2). This mechanism and quantitative measures of the circulation are discussed by Rogers & Moser (1989).

Returning to the cup-like structures shown in Fig. 2, we would like to determine their origins and the reasons for their unusual shape. First, we see that the cups that reside on the upper side of the rollers are slightly farther downstream than the lower ones. This is not a spatially-developing effect since it is also observed in the temporal case. However, the upper cups are about 25% stronger than the lower ones. This difference is not allowed by symmetry in the temporal case. The cups are clearly related to the ribs; the former lie symmetrically between the latter and slightly towards the middle of the layer. Furthermore, the sense of rotation of the ribs causes a positive spanwise strain in the regions occupied by the cups and thus creates a mechanism for the enhancement of spanwise vorticity.

However, this mechanism does not explain why the cups are concave on their inner sides, why they are strongest on the opposite side (in the streamwise sense) of the roller from the associated ribs, and why they are not convected away by the downwash (in the case of the upper cups) between the ribs. These questions are answered by examining Fig. 4. Shown there are y-z cuts of ω_3 and ω_1 at the x-location corresponding to the maximum of ω_3 in the upper cup. The ω_1 plot shows three pairs of counter-rotating structures: from top to bottom these are ribs connected to the upstream roller, opposite-signed vortices in the core

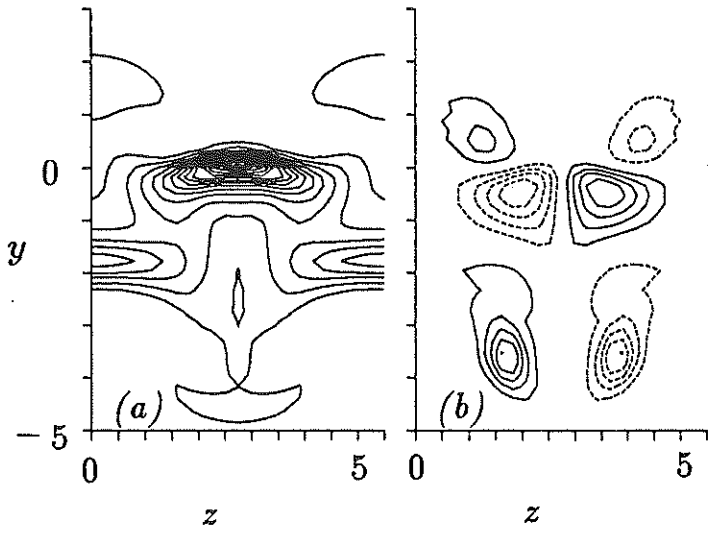

FIGURE 4. Spanwise cuts of vorticity through the roller at $x = 44$. The contour interval is 0.15, and negative values are represented by dashed lines. *(a)* $-\omega_3$, *(b)* ω_1.

of the roller (which we call "legs", a term which will become self-explanatory later), and another pair of ribs connected to the downstream roller. Each of the cups resides in the middle of a quadrapole formed by the legs and one or the other pair of ribs. The maximum amplitude of the legs is located very near the upper cup, contributing most to the positive strain there. The role of the ribs thus appears to be secondary; they contribute less to the strain, but are needed to produce a stagnation point in the vertical velocity so that the cups are not convected away and can continue to get strained. The convective effect of the strong vertical velocity created by the legs also explains the concave structure of the cups.

One would expect the upper and lower cups to be connected by vortex lines, and that these lines would show a streamwise tilt corresponding to the streamwise offset of the two cups. This is not quite true. Shown in Fig. 5 are two views of two sets of vortex lines, each set initiated in the region of maximum spanwise vorticity in each cup. A "hairpin" structure is formed by the lines, where the cups form the ends of the hairpin, and the regions between (consisting mostly of ω_1 and ω_2) are the "legs". We see that the two sets are definitely disjoint, although there is one vortex bundle (not shown) that goes from the vicinity of the downstream edge of the upper cup to the upstream edge of the lower cup. Consistent with this, all the lines are inclined by about $45-50°$, whereas a line connecting the middle of one cup to the middle of the other would be inclined

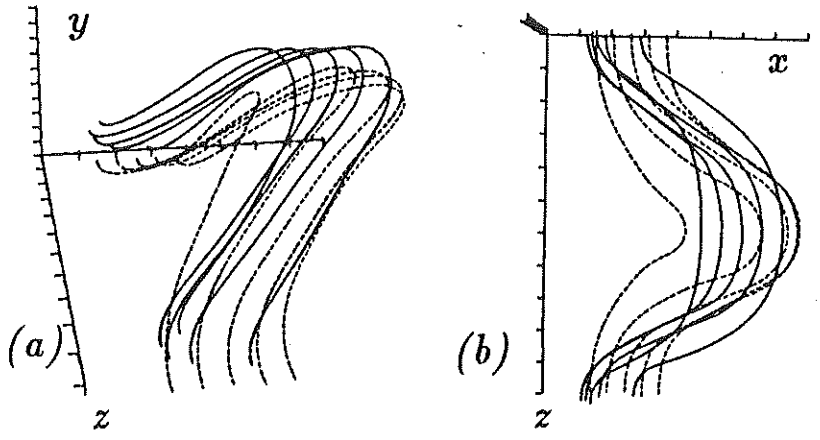

FIGURE 5. Vortex lines in the roller near $x = 42$. Dashed lines start from lower cup, solid lines from upper cup. *(a)* Perspective view, *(b)* top view.

only about 30° from the vertical. The lines emanating from the lower cup (for example) go up and forward of the upper cup so that the legs produce counter-rotating vortices just below the upper cup. Thus, vortex lines from each cup produces a strain field to enhance the other.

3.2 Passive scalar mixing

For the results discussed in this section, a passive scalar profile is specified at the inflow that is zero on the low-speed side, one on the high-speed side and has the same tanh profile as U_0 in the shear layer. It is often observed that a 2-D spatially-developing mixing layer will entrain more high-speed fluid than low-speed. The process by which this happens is shown by the passive scalar contours in Fig. 6, where $Re = 500$ and $Sc = 0.8$. When two vortices pair, they initially form an oblong structure.

As this structure turns end over end, it efficiently "engulfs" a large amount of pure fluid from both streams in the form of "tongues". We note that the low-speed tongue is narrower than the high-speed one because the proximity of an unpaired roller just upstream creates a blockage effect not present on the downstream side of the paired structure.

Furthermore, the existence of a stagnation point (in the frame moving with the vortices) between the vortices implies that the velocities associated with the tongues should be similar. Dimotakis (1986) used these arguments along with experimental data to estimate the ratio of the amount of high-speed to low-speed fluid entrained in the layer as $E = 1 + 3.9 d\delta_\omega/dx$. While it is very difficult to measure this quantity directly, the simulations show no inconsistency with it (for

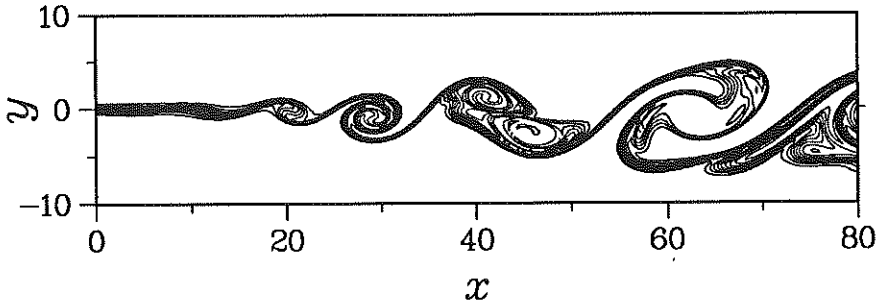

FIGURE 6. Contours of passive scalar ϕ for a 2-D mixing layer, $Re = 500$, $r = 0.2$, $Sc = 0.8$. Contour interval is 0.1.

the results reported here, $d\delta_\omega/dx \simeq 0.087$). Passive scalar contours at $Re = 200$ show similar features, although the tongues are not as distinct because of the increased diffusion.

For the 3-D case, we plot contours of the passive scalar in three $y-z$ cuts through three different braid regions in Fig. 7. This sequence shows the effect of the development of the ribs on the scalar field. In the terminology of Lin & Corcos (1984), the ribs start off in a "noncollapsed" state and only produce a mild bending of the scalar contours. After they have strengthened farther downstream, the ribs "collapse" and produce mushroom-shaped structures.

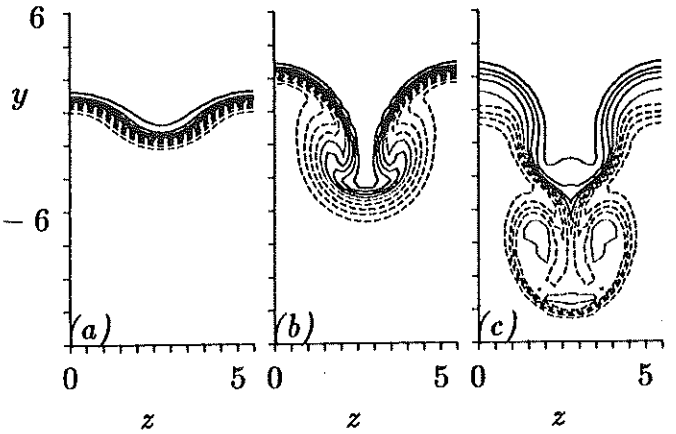

FIGURE 7. Contours of passive scalar in y-z cuts at *(a)* $x = 28$, *(b)* $x = 48$, and *(c)* $x = 63$. Contour interval is 0.1. Solid lines, $0.6 \leq \phi \leq 0.9$; dots, $\phi = 0.5$; dashes, $0.1 \leq \phi \leq 0.4$.

Analogous features are seen in the experiments of Bernal (1981). We see that there are two different kinds of mushroom structures: one falling and the other rising (which requires a periodic extension of the plots to see fully). Due to the

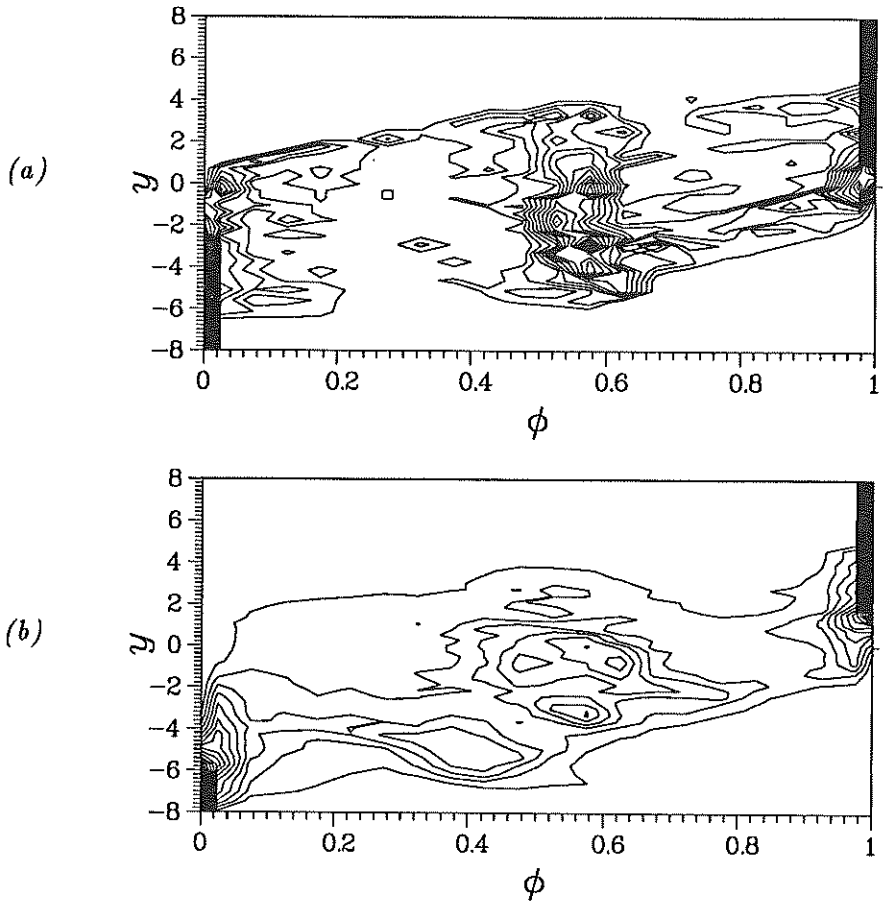

FIGURE 8. Contours of the probability density function for the passive scalar at $x = 57$. Contour difference is 0.02. *(a)* 2-D case, *(b)* 3-D case.

asymmetry of the layer, the pair of ribs associated with the latter tend to be closer together than the other pair.

This, together with the low Reynolds number of the flow, tends to "cut-off" high-speed fluid from penetrating into the core of the descending mushroom. At higher Reynolds numbers, the ribs do not interact diffusively. From the last two plots, it is clear that the ribs cause the layer to have more surface area on the low-speed side than the high-speed side. The last plot shows more low-speed fluid being entrained into the ribs and that the average value of the scalar in the core of the ribs is well below 0.5.

Statistics of the passive scalar (also called the "conserved" scalar) can be used to calculate fast-chemistry reactions. Following the analysis of Mungal & Dimotakis (1984), we assume a simple reaction $A + B \rightarrow 2P$ where the diffusivities of both reactants and the product are all equal and the reaction is very fast

compared to hydrodynamic or diffusive time scales. The equivalence ratio is defined as $\eta = c_{02}/c_{01}$, where c_{02} and c_{01} are the reactant concentrations in the low-speed and high-speed streams, respectively. The concentrations of the two reactants and the product are all related to the conserved scalar, ϕ. For the above inflow conditions, stoichiometry occurs when the conserved scalar has the value $\phi_s = \eta/(1+\eta)$. This value is called the stoichiometric mixture fraction and is also the point where the product concentration reaches a maximum. Given a probability distribution function (pdf) $p(x, y, \phi)$ of the conserved scalar, Mungal & Dimotakis (1984) showed how several quantities of interest (such as the product, product thickness, and mixture fraction derived from a "flip" experiment) can be calculated. (The pdf gives the probability that the value of the conserved scalar at (x, y) is ϕ, averaged over z and time.)

Shown in Fig. 8 are contours of pdf's for the 2-D and 3-D cases at $x = 57$. Several features are evident. Pure fluid with probability one is seen at the top-right and bottom-left of both plots. Homogeneously-mixed fluid is shown in the middle where the pdf's reach maxima between 0.5 and 0.6. In the temporal case the maxima must occur at 0.5 by symmetry. The asymmetry here is due to the 2-D "engulfment" discussed above. These maxima are nearly independent of y, as in the model of Broadwell & Breidenthal (1982). Between the homogeneous fluid in the middle and the pure fluid are "wings" in the pdfs. These are due to the strained flame sheets between the two pure fluids or between one pure fluid and the homogeneous fluid. The main difference between the 2-D and 3-D pdf's is a second maximum in the latter near $\phi = 0.4$ and for $y < 0$. This is related to the entrainment of low-speed fluid by the ribs, and (as discussed in connection with Fig. 7) is undoubtably a low Reynolds number effect.

In Fig. 9 product thickness (δ_P) normalized by the 1% visual thickness (δ_1) is plotted for the two cases. The downturn for large x for the 2-D case is due to the faster growth of the visual thickness there, while in the 3-D case the structures continue to mix the two fluids as fast as the layer grows, creating a plateau. The average mixture fraction is plotted in Fig. 10. In the laminar region (small x) the layer diffuses into the low-speed side faster than the high-speed side, lowering $\bar{\phi}$ below 0.5. At higher Reynolds numbers this quantity would be much closer to 0.5 (the difference between the two cases in this region is probably due to the thinness of the layer there and thus poor statistics). Farther downstream, the 2-D case achieves a value in the vicinity of that predicted by the Broadwell-Breidenthal model (about 0.535), while in the 3-D case $\bar{\phi}$ falls below 0.5. The latter effect is directly associated with the ribs and the second maximum in the pdf. At higher Reynolds numbers we expect that the ribs would mix fluid more symmetrically and that the second maximum would be close to 0.5. This was confirmed by a recent simulation at $Re = 400$. In this case $\bar{\phi}$ is between 0.5 and the 2-D case.

The product thickness as a function of the stoichiometric mixture fraction at

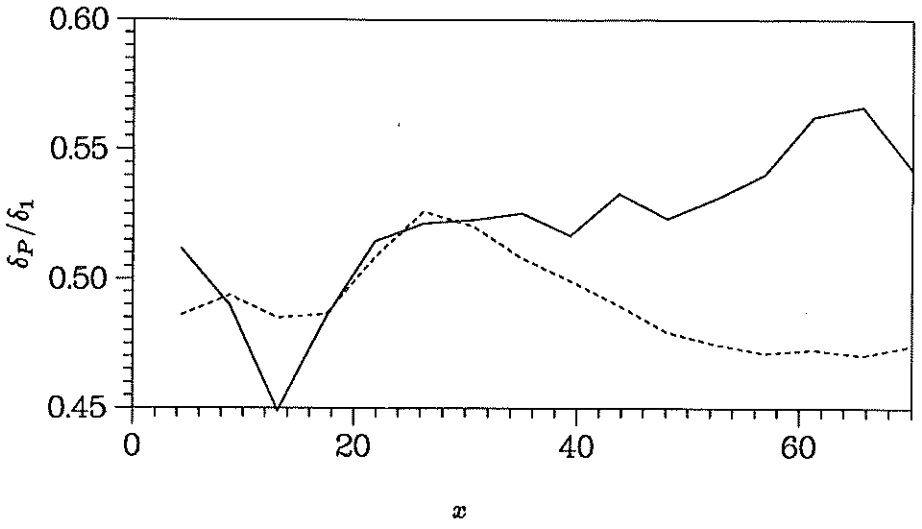

FIGURE 9. Product thickness normalized by visual thickness. Solid line, 2-D; dashed line, 3-D.

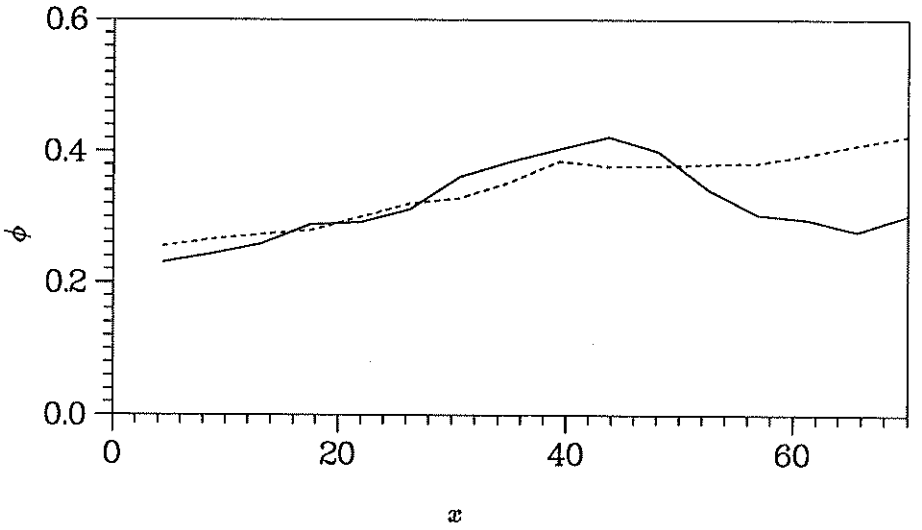

FIGURE 10. Mixture fraction. Solid line, 2-D; dashed line, 3-D.

$x = 57$ is compared to the experimental results (at $r = 0.38$) of Mungal & Dimotakis (1984) in Fig. 11. The 2-D results are just slightly below the experimental measurements for all values of ϕ_s, while the 3-D results are above. For small ϕ_s (low-speed reactant lean), excessive product is created in the latter case due to the effect of the ribs. It is not clear to what extent the close comparison in the

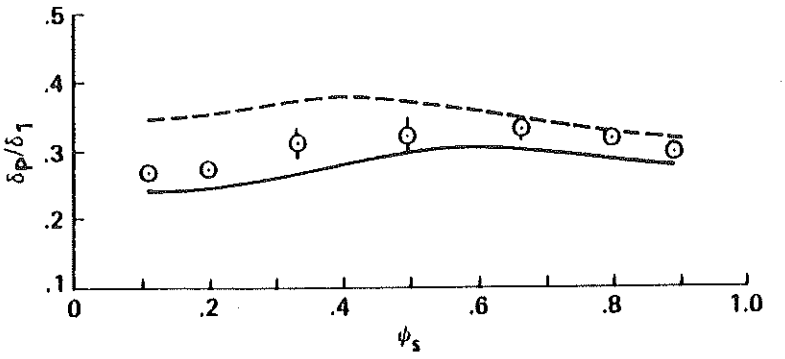

FIGURE 11. Product thickness/visual thickness vs. stoichiometric mixture fraction. Solid line, 2-D; dashed line, 3-D; symbols, experimental data from Mungal & Dimotakis (1984).

2-D case is fortuituous; the extra diffusion from the low Reynolds number here appears to balance the small-scale motion and mixing in the turbulent experiments. The $Re = 400$ product thickness (not shown) is closer to the experiments than the lower Re results, especially for small ϕ_s.

4. Wakes

In this section some results from simulations of spatially-developing wakes will be discussed. We will concentrate on the effects of 3-D perturbations on a plane Gaussian wake at a moderate Reynolds number. Very few 3-D simulations of wakes have been performed in the past. Riley & Metcalfe (1980) performed a direct numerical simulation of the temporally-developing turbulent wake of an axisymmetric body using experimental data for the initial conditions. Although the mesh was coarse, low-order statistics compared well with the experiments. Meiburg & Lasheras (1988) reported results from wake experiments with different types of spanwise forcing and computed the flow using inviscid vortex dynamics calculations. It is difficult to use the latter to study small-scale details of free-shear flows, but they were able to reproduce the large-scale features of the experiments. More recently, Chen *et al.* (1989) performed well-resolved simulations of a compressible plane wake. Their main goal was to determine the effect of Mach number on the development of the wake, but they also described the development of 3-D structures which should be similar to the incompressible case.

In this work we present results for a relatively simple case where two different kinds of perturbations are added to a Gaussian mean inflow profile. The first is a two-dimensional (2-D) time-periodic forcing where the profiles for u and v are the eigenfunctions of the corresponding Rayleigh equations. Any frequency near the most amplified one produces the classical Kármán vortex street. The second kind of perturbation is a spanwise-periodic array of counter-rotating streamwise

vortices. These are assumed to be steady as they might be in a wind tunnel with small nonuniformities in the last screen. As in the mixing layer and other shear flows, the streamwise vortices (*ribs*) are amplified by the strain field of the 2-D spanwise vortices (*rollers*). When the ribs become sufficiently strong, they distort the rollers through advection and strain effects. These effects will be contrasted with a 2-D simulation *sans* ribs. In addition, a passive scalar with a Gaussian profile is introduced at the inflow. It is often assumed in the experimental literature that smoke or heat introduced in the wake will follow the vorticity. The degree to which this is true will be tested in both the 2-D and 3-D simulations.

The Reynolds number is $Re = U_0\delta/\nu = 400$, where δ is the half-width of the layer at the inflow. The inflow profile is defined by $\bar{U}(y) = 1 - \lambda \exp(-.69315y^2)$, where $\lambda = 0.692$ is the velocity defect (corresponding to the experiments of Sato & Kuriki 1961). The Schmidt number is $Sc = 1$. The 2-D forcing is applied at a frequency of 0.5 and an amplitude of 0.06. The maximum growth rate occurs at a frequency of 0.614, but the lower value was used to compensate for the viscous thickening of the wake downstream. For the 3-D simulation steady profiles for v and the spanwise velocity w are added at the inflow to produce streamwise vorticity with an amplitude of 0.1 and a spanwise wavelength of 6. As with the mixing layer calculations, each velocity component is required to satisfy a convective outflow boundary condition, except here we use $c = 0.9$. At infinity, all perturbations are set to zero. The length of the computational domain is $L_x = 70$ and the vertical mapping parameter is $\beta = 6$. The mesh is $384 \times 128 \times 24$ (grid points in x, Fourier modes in y and z). Most of the aliasing errors were eliminated by using a collocation grid in the spectral directions of 160×32.

Shown in Fig. 12 are contours of spanwise vorticity (ω_3) for the base-line 2-D case. The formation of a vortex street consisting of alternating-sign vortices (rollers) is clearly seen. A consequence of conservation of angular momentum is the formation of "spiral arms" around each vortex; not all the vorticity can roll up into the vortex cores. Farther downstream these arms diffuse away, leaving nearly circular vortex cores. Note also the near-symmetry between the upper and lower vortices.

Contours of ω_3 for the 3-D case are plotted in Fig. 13 in the two x-y symmetry planes (where $\omega_1 = 0$). These planes are each between a pair of counter-rotating streamwise vortices. Qualitatively the same structures appear as in the 2-D case, but there are important quantitative differences. Considering the row of vortices along the top (negative ω_3), we see that the flow starts off very much like the 2-D flow, but by $x = 20$ significant distortion in z appears. At $z = 0$ the peak vorticity is on the inside edge of the rollers, while at $z = 3$ the peak vorticity is on the outside edge. This cannot be an advection effect since by $x \simeq 40$ the peak value of ω_3 reaches -0.8 (at the inflow it is about -0.5). Thus the variation in z must be due to vortex stretching effects. This enhancement

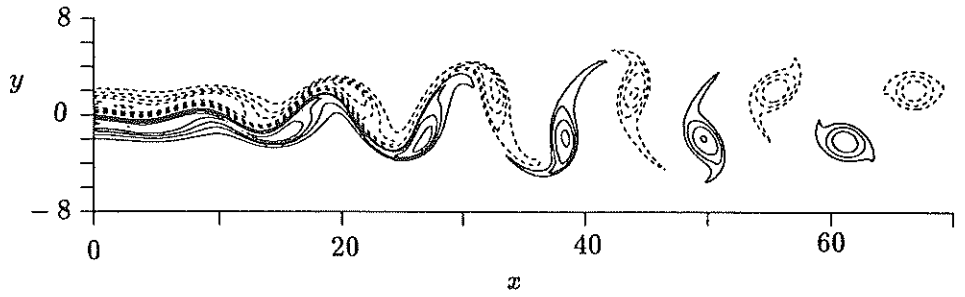

FIGURE 12. Contours of spanwise vorticity for the 2-D case. Contour interval is 0.1. Dashed lines denote negative levels, solid lines denote positive levels.

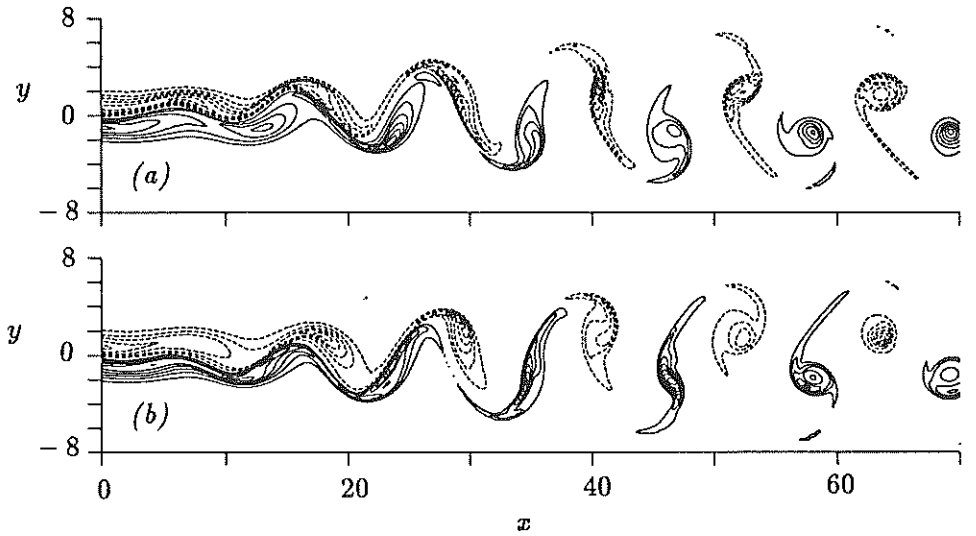

FIGURE 13. Contours of spanwise vorticity for the 3-D case at *(a)* $z = 0$ and *(b)* $z = 3$. Contour interval is 0.1.

of vorticity occurs at all z locations but is most pronounced at $z = 0$. Beyond $x \simeq 35$, a different process from the one responsible for the above enhancement becomes dominant. At $z = 3$, the maximum vorticity amplitude drops suddenly by $x = 40$, then rises to nearly its previous level by $x = 60$. At $z = 0$, a small, intense and nearly symmetric elliptic roller forms by $x = 40$. This is followed by a suppression of vorticity on one side of the center of the roller so that a nearly irrotational region is imbedded inside the roller by $x = 60$. Because of the symmetry in the inflow conditions, all of the above comments for the upper row of vortices at $z = 0$ and $z = 3$ apply to the mirror image in y of the lower row at $z = 3$ and $z = 0$, respectively.

Some of the mechanisms for the enhancement and suppression of ω_3 in certain regions are evident from an examination of the streamwise (ω_1) and vertical (ω_2)

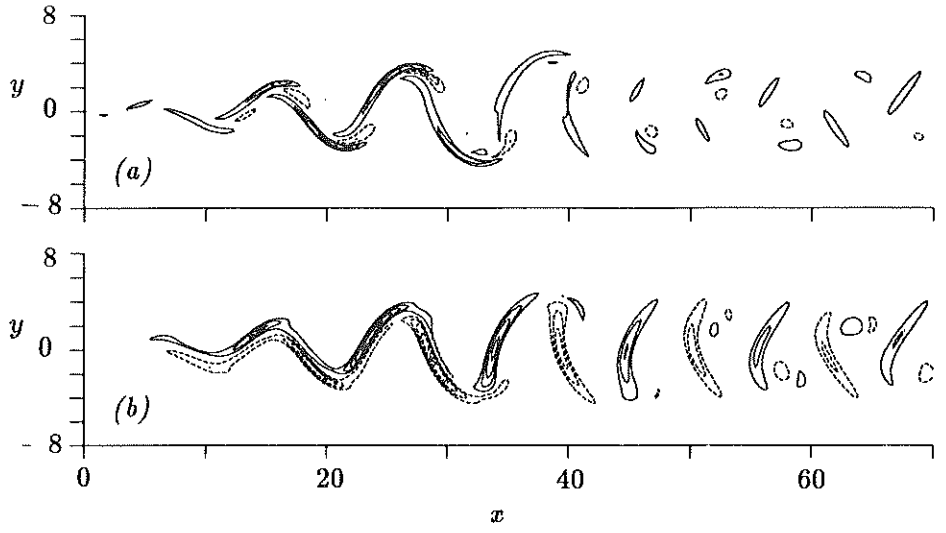

FIGURE 14. Contours of *(a)* streamwise vorticity and *(b)* vertical (cross-stream) vorticity corresponding to Fig. 2 at $z = 1.5$ Contour interval is 0.1.

components of vorticity, shown in Fig. 14 at $z = 1.5$. Both components develop very quickly up to about $x = 25$, then decay slowly thereafter. At $z = 1.5$, ω_1 is positive at the inflow and leads directly to the formation of ribs with the same sign. These ribs can be divided into two sets; those with positive ω_2 and those with negative. For $x < 20$ the former are clearly associated with the upper rollers and the latter with the lower rollers. During the growth phase of the ribs, they connect spanwise vortices of like sign (see Chen *et al.* 1989).

As in mixing layers, the ribs are intensified by the 2-D strain field of the main rollers, but again this mechanism cannot increase the circulation around a rib. We find that the same mechanism as in the mixing layer is responsible for converting ω_3 into ω_1. However, the process is less efficient as the layer develops since the 2-D strain field between rollers is weakened by the presence of both signs of ω_3 in alternate rollers. In Fig. 13 note that the main effect of the 3-D distortion of ω_3 for $x < 35$ is the enhancement of vorticity along one side of a roller and suppression along the opposite side (both due to the vortex stretching terms produced by the ribs), thus shifting the peak vorticity towards one side. In the z-plane on the other side of a particular streamwise vortex, the peak vorticity is shifted to the other side of the same spanwise roller. Due to this distortion, the vortex lines in the rollers will have an x (as well as a y) component. Farther downstream, one end of each rib becomes increasingly associated with a roller on the opposite side of the wake. Also, they tend to stand nearly vertical, in contrast to a typical rib angle of 45° for $x < 25$ and for mixing layers. This transition coincides with the end of the growth of the ribs and the beginning of their decay.

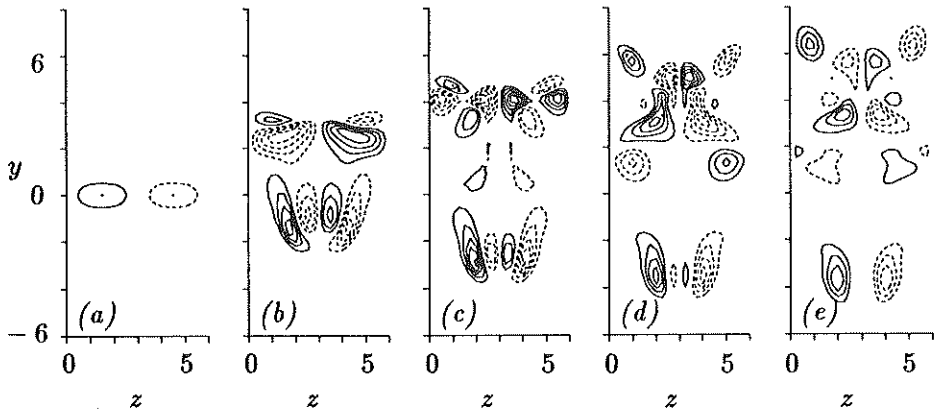

FIGURE 15. Contours of streamwise vorticity in z-y planes at *(a)* $x = 0$, *(b)* $x = 29$, *(c)* $x = 40.5$, *(d)* $x = 52$, and *(e)* $x = 63.5$. Contour interval is 0.05.

Shown in Fig. 15 are spanwise (z-y) cuts of ω_1 at five x locations. The first plot shows the inflow forcing, and the others show cuts through the upper rollers. Note that in either half of the domain (*e.g.*, $0 \leq z \leq 3$), the magnitudes of the positive and negative streamwise vorticity are about the same even though there is only one sign at the inflow. For $x < 40$ the ribs (the lowest and highest pairs of vortices in Figs. 15(*b-e*)) have the characteristic shape of "non-collapsed" vortices – elliptical and tilted from the horizontal (see Lin & Corcos 1984). This is a relatively stable state. Farther downstream they begin to show signs of collapse to small, round and more intense vortices (however, a higher Reynolds number is needed to see this clearly). Comparing Figs. 14(*a*) and 14(*b*) at $x = 29$ to Fig. 15(*b*) we note that the regions of enhanced ω_3 are located in the middle of positive strain regions created by ω_1-quadrapoles. Similarly, regions of ω_3 suppression are also located in the middle of quadrapoles, but where the strain is negative. Further, half of the ω_1 vorticity involved is associated with ribs while the other half is due to the distortion of the rollers. By $x = 40$ (Fig. 15(*c*)), several changes in the structure of the flow have occurred. The ribs and rollers have moved away from one another so that the former are not a part of one of the above-mentioned quadrapoles and do not appear to significantly contribute to the strain in the vicinity of the rollers. Instead, new ω_1 is created within the rollers, which are then strained in a different manner than before. One can follow the evolution of ω_1 and see that the quadrapoles it forms are responsible for the changing distribution and intensity of ω_3.

A perspective view (Fig. 16) of the rollers located between $x = 40$ and $x = 60$ shows part of the evolution of ω_3. In Fig. 17 two perspective views of vortex lines initiated in the ribs located at $x = 28$ and $x = 34$ show the formation of vortex loops. Since both signs of ω_3 are needed to close the loops, the ribs must connect opposite-signed vortices. Farther upstream, vortex lines continue all the way across the span and are not closed, suggesting the ribs connect vortices

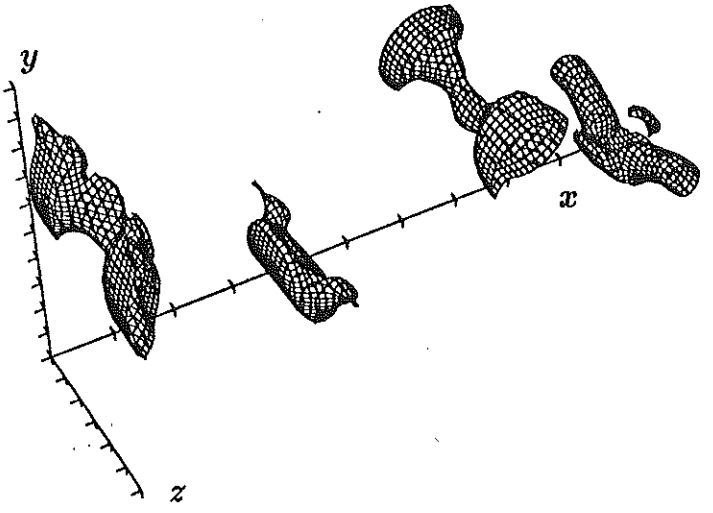

FIGURE 16. Perspective view of $|\omega_3|$ corresponding to figure 14 in the range $40 \leq x \leq 60$. Contour level is 0.35.

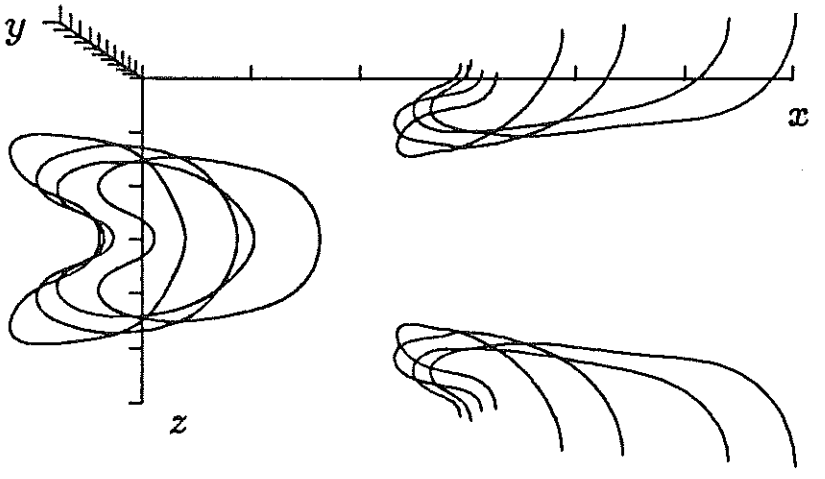

FIGURE 17. Top view of vortex lines initiated in the ribs at $x = 28$ and $x = 34$. x axis extent is $28 \leq x \leq 40$.

of like sign. We note also that the vortex loops originally associated with the bottom half of the wake (one of which is shown at the left in the plots of Fig. 17) are all lined up and centered at $z = 3$ while the upper ones are centered at $z = 0$

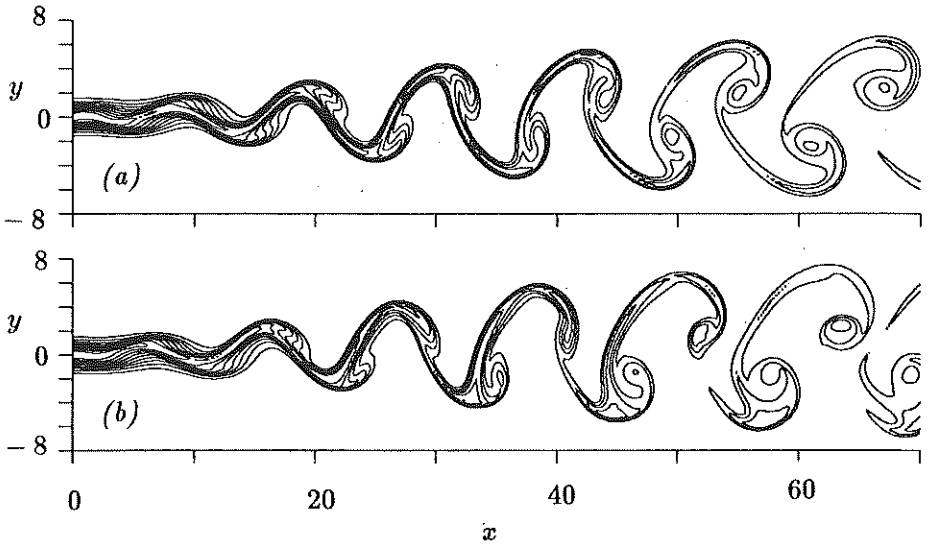

FIGURE 18. Passive scalar contours for the *(a)* 2-D case, and *(b)* 3-D case at $z = 0$. Contour interval is 0.1.

(or, equivalently, $z = 6$). Introducing time-periodicity into ω_1 at the inflow will create other patterns of loops.

Experimentally, one often introduces smoke or heat as a passive scalar into the wake in order to trace the vorticity. Of course, this is only an approximation unless the flow is 2-D, the Schmidt number is unity, and the inflow passive scalar profile is identical to the vorticity profile. We tested this approximation here for both the 2-D and 3-D cases, using a Gaussian profile (with half-width 0.833) to model the injection of a passive scalar. Shown in Fig. 18 are the results for the 2-D case and for the 3-D case at $z = 0$. Comparing Figs. 12 and 18(a) we see significant differences. However, for $x > 45$, the maxima of the passive scalar lie very close to the extrema in vorticity, but with no consistent relative offset. For the 3-D case, a comparison of Figs. 14(a) and 18(b) shows larger differences. In particular, the upper and lower sides are less similar in the passive scalar than in the vorticity. Also, while there is a local maxima in the passive scalar near each roller, there are also concentrations of scalar in nearly irrotational areas as well. This may be an indication of history effects; the passive scalar may concentrate in regions of high vorticity, and then be left behind as the vorticity moves elsewhere through vortex-stretching effects.

REFERENCES

BERNAL, L. P. 1981 thesis, California Institute of Technology, Pasadena, CA.

BROADWELL, J. E. & BREIDENTHAL, R. E. 1982 *J. Fluid Mech.* **125**, 397–410.

BROWN, G. L. & ROSHKO, A. 1974 *J. Fluid Mech.* **64**, 775–816.

BUELL, J. C. 1989 submitted to *J. Comp. Phys.*

BUELL, J. C. & HUERRE, P. 1988 in *Proceedings of the 1988 Summer Program*, Center for Turbulence Research, p. 19.

CHEN, J. H., CANTWELL, B. J. & MANSOUR, N. N. 1989 AIAA Paper No. 89-0285, Reno.

COMTE, P., LESIEUR, M., LAROCHE, H. & NORMAND, X. 1987 in *Turbulent Shear Flows VI*, Springer-Verlag.

DAVIS, R. W. & MOORE, E. F. 1985 *Phys. Fluids* **28**, 1626–1635.

DIMOTAKIS, P. E. 1986 *AIAA J.* **24**, 1791–1796.

HO, C.-M. & HUERRE, P. 1984 *Ann. Rev. Fluid Mech.* **16**, 365–424.

HUANG, L. S. & HO, C.-M. 1989 submitted to *J. Fluid Mech.*

KONRAD, J. H. 1976 thesis, California Institute of Technology, Pasadena, CA.

KOOCHESFAHANI, M. M. & DIMOTAKIS, P. E. 1986 *J. Fluid Mech.* **170**, 83–112.

LASHERAS, J. C., CHO, J. S. & MAXWORTHY, T. 1986 *J. Fluid Mech.* **172**, 231–258.

LELE, S. K. 1989 submitted to *J. Comp. Phys.*

LIN, S. J. & CORCOS, G. M. 1984 *J. Fluid Mech.* **141**, 139–178.

LOWERY, P. S. 1986 thesis, Stanford University, Stanford, CA.

MEIBURG, E. & LASHERAS, J. C. 1988 *J. Fluid Mech.* **190**, 1–37.

MUNGAL, M. G. & DIMOTAKIS, P. E. 1984 *J. Fluid Mech.* **148**, 349–382.

PIERREHUMBERT, R. T. & WIDNALL, S. E. 1982 *J. Fluid Mech.* **114**, 59–82.

ROGERS, M. M. & MOSER, R. D. 1989 Proceedings of the Seventh Symposium on Turbulent Shear Flows, Stanford, CA.

RILEY, J. J. & METCALFE, R. W. 1980 Turbulent Shear Flows 2, 78–97.

SATO, H. & KURIKI, K. 1961 *J. Fluid Mech.* **11**, , 321–352.

WRAY, A. A. 1988 submitted to *J. Comp. Phys.*